

# Lawrence Berkeley National Laboratory

## LBL Publications

### Title

Toward MBenes Battery Electrode Materials: Layered Molybdenum Borides for Li-Ion Batteries

### Permalink

<https://escholarship.org/uc/item/8x32b855>

### Journal

Small Methods, 7(8)

### ISSN

2366-9608

### Authors

Majed, Ahmad

Torkamanzadeh, Mohammad

Nwaokorie, Chukwudi F

et al.

### Publication Date

2023-08-01

### DOI

10.1002/smtd.202300193

### Copyright Information

This work is made available under the terms of a Creative Commons Attribution License, available at <https://creativecommons.org/licenses/by/4.0/>

Peer reviewed

# Toward MBenes Battery Electrode Materials: Layered Molybdenum Borides for Li-Ion Batteries

Ahmad Majed, Mohammad Torkamanzadeh, Chukwudi F. Nwaokorie, Karamullah Eisawi, Chaochao Dun, Audrey Buck, Jeffrey J. Urban, Matthew M. Montemore, Volker Presser, and Michael Naguib\*

Lithium-ion and sodium-ion batteries (LIBs and SIBs) are crucial in our shift toward sustainable technologies. In this work, the potential of layered boride materials (MoAlB and Mo<sub>2</sub>AlB<sub>2</sub>) as novel, high-performance electrode materials for LIBs and SIBs, is explored. It is discovered that Mo<sub>2</sub>AlB<sub>2</sub> shows a higher specific capacity than MoAlB when used as an electrode material for LIBs, with a specific capacity of 593 mAh g<sup>-1</sup> achieved after 500 cycles at 200 mA g<sup>-1</sup>. It is also found that surface redox reactions are responsible for Li storage in Mo<sub>2</sub>AlB<sub>2</sub>, instead of intercalation or conversion. Moreover, the sodium hydroxide treatment of MoAlB leads to a porous morphology and higher specific capacities exceeding that of pristine MoAlB. When tested in SIBs, Mo<sub>2</sub>AlB<sub>2</sub> exhibits a specific capacity of 150 mAh g<sup>-1</sup> at 20 mA g<sup>-1</sup>. These findings suggest that layered borides have potential as electrode materials for both LIBs and SIBs, and highlight the importance of surface redox reactions in Li storage mechanisms.

13.0% from 2020 to 2027.<sup>[2]</sup> Lithium, among other alkali metals, has been studied the most due to its relatively small atomic size, mass, and higher ion mobility, giving batteries with higher energy storage capacity.<sup>[3]</sup>

2D nanosheets are potentially suitable active materials for hosting ions generally due to their higher surface areas, favorable diffusion kinetics, and higher ion capacities owing to their unique morphology.<sup>[4]</sup> Transition metal borides (TMBs), such as MoB<sub>2</sub>, TiB<sub>2</sub>, NbB<sub>2</sub>, ReB<sub>2</sub>, and OsB<sub>2</sub>, are considered refractory materials because of their high chemical, mechanical, and thermal stability.<sup>[5]</sup> This family has unique mechanical, electronic, and thermal properties, broadening the range of applications to include tribology,<sup>[6]</sup> electrochemical energy storage,<sup>[7]</sup> catalysis,<sup>[8]</sup>

and high-temperature structures in the aerospace industry.<sup>[9]</sup> Ternary transition metal borides, such as MoAlB, Cr<sub>2</sub>AlB<sub>2</sub>, Mn<sub>2</sub>AlB<sub>2</sub>, and Fe<sub>2</sub>AlB<sub>2</sub>, are considered layered materials with an orthorhombic crystal structure that can be described as blocks of TMB (e.g., MoB and FeB) interleaved by aluminum atoms (double layers of Al in the case of MoAlB, mono layers for the rest).<sup>[10]</sup>

## 1. Introduction

Lithium-ion batteries (LIBs), owing to their relatively high energy and power density, are commonly used within portable applications such as mobile phones and laptops. Since Sony started using LIBs in the 1990s,<sup>[1]</sup> exponential growth in manufacturing batteries reached a current market size of \$34.2 billion (USD), which is expected to grow at a compound annual growth rate of

A. Majed, K. Eisawi, A. Buck, M. Naguib  
Department of Physics and Engineering Physics  
Tulane University  
New Orleans, LA 70118, USA  
E-mail: naguib@tulane.edu


M. Torkamanzadeh, V. Presser  
INM – Leibniz Institute for New Materials  
66123 Saarbrücken, Germany

M. Torkamanzadeh, V. Presser  
Department of Materials Science and Engineering  
Saarland University  
66123 Saarbrücken, Germany

C. F. Nwaokorie, M. M. Montemore  
Department of Chemical and Biomolecular Engineering  
Tulane University  
New Orleans, LA 70118, USA

C. Dun, J. J. Urban  
The Molecular Foundry  
Lawrence Berkeley National Laboratory  
Berkeley, CA 94720, USA

V. Presser  
saarene – Saarland Center for Energy Materials and Sustainability  
66123 Saarbrücken, Germany

 The ORCID identification number(s) for the author(s) of this article can be found under <https://doi.org/10.1002/smt.202300193>

© 2023 The Authors. Small Methods published by Wiley-VCH GmbH. This is an open access article under the terms of the Creative Commons Attribution-NonCommercial License, which permits use, distribution and reproduction in any medium, provided the original work is properly cited and is not used for commercial purposes.

DOI: 10.1002/smt.202300193

MBene is a term derived from MXene (M: early transition metal, X: C and/or N), given their similarities to graphene from morphological and high electrical conductivity aspects,<sup>[11,12]</sup> with one change where X is boron.<sup>[13]</sup> Combining first-principles density functional method and crystal structure prediction techniques, Bo et al. reported a group of hexagonal 2D MBenes, transition metal borides such as Sc<sub>2</sub>B<sub>2</sub>, Ti<sub>2</sub>B<sub>2</sub>, Y<sub>2</sub>B<sub>2</sub>, Zr<sub>2</sub>B<sub>2</sub>, and Mo<sub>2</sub>B<sub>2</sub>, that are predicted to have good stability and excellent electronic conductivity.<sup>[14]</sup> It was also predicted that MBenes like V<sub>2</sub>B<sub>2</sub>, Cr<sub>2</sub>B<sub>2</sub>, Mn<sub>2</sub>B<sub>2</sub>, Mo<sub>2</sub>B<sub>2</sub>, and Fe<sub>2</sub>B<sub>2</sub> have promising performance as electrode materials in LIBs and/or sodium-ion batteries.<sup>[12,15]</sup> Mo<sub>2</sub>B<sub>2</sub> and Fe<sub>2</sub>B<sub>2</sub> were predicted to have low omnidirectional diffusion energy barriers and high specific capacity for Li atoms.<sup>[12]</sup>

In the Mo–B binary phase diagram, Mo borides have many possible compositions, such as Mo<sub>2</sub>B, MoB, MoB<sub>2</sub>, Mo<sub>2</sub>B<sub>3</sub>, and MoB<sub>4</sub>.<sup>[16]</sup> For MoB, there are two possible phases: tetragonal  $\alpha$ -MoB (*I*4<sub>1</sub>/amd, *Z* = 8) and orthorhombic  $\beta$ -MoB (*Cmcm*, *Z* = 4). However,  $\beta$ -MoB was found to be slightly less stable than  $\alpha$ -MoB, which explains why  $\beta$ -MoB can only be synthesized at low temperatures.<sup>[16]</sup> Similar to the synthesis of MXenes from MAX phases using selective etching of the A element layer,<sup>[17]</sup> in principle, 2D  $\beta$ -MoB nanosheets can be realized by the selective etching of Al from MoAlB at relatively low temperatures to maintain the structure of the MoB building blocks. Using ab initio calculations, Guo et al. reported that 2D Mo<sub>2</sub>B<sub>2</sub> with van der Waals bonding between the atomic layers could be achieved through selective etching of the single Al layer from Mo<sub>2</sub>AlB<sub>2</sub>, which could be a potential MBene precursor.<sup>[12]</sup> However, since Mo<sub>2</sub>AlB<sub>2</sub> is metastable, one has to start with MoAlB (despite having double Al layers) as it is the only stable phase that can be obtained by a solid-state synthesis in the Mo–Al–B ternary phase diagram.<sup>[18]</sup>

Partial etching of MoAlB was first reported in 2017, where the powdery sample was stirred in NaOH solutions of different concentrations (10% and 30%), etching times (24 and 72 h), and temperatures (room temperature and 70 °C).<sup>[19]</sup> The best results were achieved by stirring MoAlB in 10% NaOH at room temperature for 24 h. The effects of concentration and etching time were not significant, while raising the etching temperature to 70 °C or replacing the etchant with 48% HF caused significant corrosion.<sup>[19]</sup> After the NaOH treatment, it was observed that Al was etched out of the surface of the particles only, as the formed MoAl<sub>1-x</sub>B hinders further etching. To obtain crystalline Mo<sub>2</sub>AlB<sub>2</sub>,<sup>[20]</sup> the already NaOH-treated MoAlB powders were pressed, vacuum-sealed into quartz ampules, and then heated to 600 °C for 4.5 h; the heating cycle was ended by quenching since Mo<sub>2</sub>AlB<sub>2</sub> is metastable.<sup>[20]</sup> Alameda et al. also reported that using 2 m LiF and 6 m HCl at room temperature results in similar outcomes to using 10% NaOH.<sup>[21]</sup> Through optimization of the synthetic parameters, Kim et al. reported a phase-pure Mo<sub>2</sub>AlB<sub>2</sub> by etching MoAlB in 3 m LiF and 10 m HCl at 40 °C for 48 h, though they did not further explore the conversion of Mo<sub>2</sub>AlB<sub>2</sub> into 2D MBene.<sup>[22]</sup>

As outlined above, the etching and exfoliating MAB phases into 2D MBenes have been shown to be synthetically elusive,<sup>[21,23]</sup> hence the scarce experimental reports on their applications.<sup>[24]</sup> While general aspects of Mo<sub>2</sub>AlB<sub>2</sub> synthesis and the resulting partially-etched species were investigated in past works, their actual use for Li-ion batteries has remained unexplored. In this

study, we report synthesizing single-phase Mo<sub>2</sub>AlB<sub>2</sub> and its electrochemical performance as electrode materials for Li-ion and Na-ion batteries for the first time. At a specific current of 20 mA g<sup>-1</sup>, a specific capacity of 380 mAh g<sup>-1</sup> (corresponding to 2.7 Li per 1 Mo<sub>2</sub>AlB<sub>2</sub>) was achieved. The lithiation and delithiation mechanisms were studied through X-ray photoelectron spectroscopy (XPS) to confirm the intrinsic electrochemical properties of the structure in our study.

## 2. Results and Discussion

The MoAlB structure can be viewed as Mo<sub>2</sub>B<sub>2</sub>-2Al-Mo<sub>2</sub>B<sub>2</sub>, where each Mo<sub>2</sub>B<sub>2</sub> atomic layer is interleaved with double zigzag Al layers while Mo<sub>2</sub>AlB<sub>2</sub> has only one Al layer, as shown in the schematic view in **Figure 1a**. The solid-state synthesis of MoAlB was confirmed by comparing the X-ray diffractogram in **Figure 1b** to the reflections predicted for MoAlB (PDF#01-072-1277). The as-synthesized MoAlB pellet was pulverized into powders, poured into HF acid, stirred at 45 °C for 48 h, washed with de-ionized water, and dried using vacuum-assisted filtration to obtain Mo<sub>2</sub>AlB<sub>2</sub>. Energy dispersive X-ray spectroscopy (EDS) of the treated sample showed Mo:Al to be 2:1 (atomic ratio) after etching, indicating 50% Al reduction. To confirm the topochemical transformation of MoAlB into Mo<sub>2</sub>AlB<sub>2</sub>, XRD patterns of the two samples were collected. As shown in **Figure 1b**, a significant change in the structure is noticed. The inset of **Figure 1b** shows the (020) reflection shift due to etching from 12.6° (*2* $\theta$ ) to 13.8° (*2* $\theta$ ), indicating a reduction in *d*-spacing from  $\approx$ 7.0 to 6.4 Å and removal of an Al layer, which was also reported in the previous literature.<sup>[19–22,25]</sup> Alameda et al.<sup>[20]</sup> utilized annular dark-field in the scanning transmission electron microscope to investigate the structural transformation from MoAlB to Mo<sub>2</sub>AlB<sub>2</sub>. Their findings indicated that the double Al layers are reduced to a singular layer upon etching, and that the layered structure is made of [Al–(Mo<sub>2</sub>B<sub>2</sub>)]<sub>*n*</sub> blocks. The researchers also observed that the nanolaminar sheets have varying thicknesses ranging from 1 to 3 unit cells of Mo<sub>2</sub>AlB<sub>2</sub>, with the majority of the sheets having a thickness of 1 unit cell ( $\approx$ 1.3 nm). **Figure 1c** shows a scanning electron micrograph of Mo<sub>2</sub>AlB<sub>2</sub>, revealing accordion-like flakes with a layered morphology similar to MXenes.<sup>[17]</sup>

From previous literature, particle size selection was reported to affect etching quality.<sup>[20,26]</sup> Therefore, we separated the precursor MoAlB sample sizes into two ranges, namely, small ( $\leq$ 10  $\mu$ m) and large (10 to 45  $\mu$ m) particles. Results after applying HF treatment to both samples can be found in **Figure S1** and **Table S1**, Supporting Information. The larger particle size range showed a larger shift in the (020) peak in **Figure S1a**, Supporting Information, less Al% content in the EDS results, higher mass loss of 30% for (10 to 45  $\mu$ m) and 15% for ( $\leq$ 10  $\mu$ m), and an accordion-like morphology, **Figure S1c**, Supporting Information. Therefore, larger particles (10 to 45  $\mu$ m) are expected to have a better etching response from the HF treatment etching compared to smaller ( $\leq$ 10  $\mu$ m) particles. This could be due to the easier passivation of smaller particles,<sup>[27]</sup> or due to the higher reactivity of smaller particles with larger surface area raising the possibility that they are etched then dissolved completely in HF, which can be observed during the washing step when a dark purple colored solution appears, indicating the existence of Mo<sup>3+</sup> in the solution. The lower mass loss of particles  $\leq$ 10  $\mu$ m suggests a combined mechanism

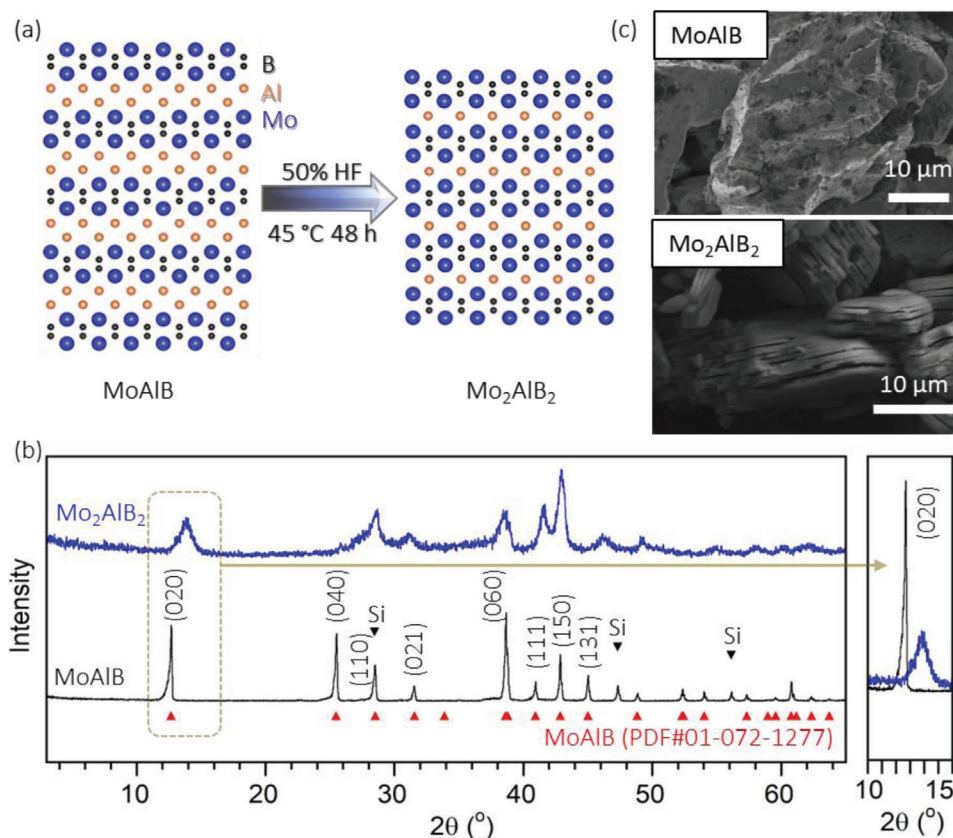


**Figure 1.** From MoAlB to Mo<sub>2</sub>AlB<sub>2</sub>: a) Schematic for the structural evolution of Mo<sub>2</sub>AlB<sub>2</sub> from MoAlB. b) X-ray diffractograms of MoAlB before and after HF treatment. Si was added as an internal reference for the peak position. c) Scanning electron micrograph of MoAlB before and after etching.

where small particles become passivated or fully etched. From these results, we can recommend using size selection to target larger particles before etching to narrow the particle size distribution and increase the etching efficiency. For further tests in this study, we focused on the (10 to 45  $\mu\text{m}$ ) sample. After etching, we milled the Mo<sub>2</sub>AlB<sub>2</sub> powder (scanning electron micrographs are shown in Figure S2, Supporting Information) to explore the milling effect on the electrochemical performance.

The electrochemical behavior of Mo<sub>2</sub>AlB<sub>2</sub> as an electrode material for LIBs is shown in Figure 2 and Figures S3–S7, Supporting Information, and for Na-ion batteries (SIBs) the electrochemical behavior is shown in Figure S8, Supporting Information. The cyclic voltammograms of MoAlB and Mo<sub>2</sub>AlB<sub>2</sub> at 0.2 mV s<sup>-1</sup> scan rate in Figure 2a show a significant difference. Specifically, there are two redox pairs at (0.39 and 0.45 V) versus Li/Li<sup>+</sup> and (1.25 and 1.52 V) versus Li/Li<sup>+</sup> appearing after HF etching, indicating that more electroactive species existed. The redox peaks of the electrodes before etching were at potentials below 0.1 V versus Li/Li<sup>+</sup>, which are related to the activated carbon suggesting that MoAlB is not electrochemically active.<sup>[28]</sup> The redox peak positions in the cyclic voltammograms after milling remained unchanged. Figure S3, Supporting Information, shows the first four cycles in milled Mo<sub>2</sub>AlB<sub>2</sub>. The first discharge had relatively more peaks due to irreversible reactions and likely the formation of solid electrolyte interphase (SEI). Potentiostatic electrochemical impedance spectroscopy (PEIS) of MoAlB, Mo<sub>2</sub>AlB<sub>2</sub>,

and milled Mo<sub>2</sub>AlB<sub>2</sub> are shown in Figure S4a, Supporting Information, along with their fits. The circuit used in fitting the PEIS data is shown in Figure S4c, Supporting Information. Etching appeared to reduce the charge transfer resistance  $R_{ct}$  from 3.9 to 3.2 m $\Omega$  cm<sup>2</sup> without significantly affecting the system resistance  $R_s$  from 0.64 (MoAlB) to 0.7 m $\Omega$  cm<sup>2</sup> (Mo<sub>2</sub>AlB<sub>2</sub>). Etching also reduced the slope of the straight line at the lower frequency region, indicating a more diffusion-limited regime is accessed, which agrees with the results from the  $b$ -value. Milling Mo<sub>2</sub>AlB<sub>2</sub> showed more deviation toward the diffusion regime with a slight increase in the resistances  $R_s = 1.1$  m $\Omega$  cm<sup>2</sup> and  $R_{ct} = 3.9$  m $\Omega$  cm<sup>2</sup>.

A range of scan rates (namely, 0.1, 0.2, 0.5, 1.0, and 2.0 mV s<sup>-1</sup>), was tested for the electrodes before etching, after etching, and after milling of the etched material (Figure S3a–c, Supporting Information). Higher current values are usually observed for faster scan rates due to the decrease in the size of the diffusion layer.<sup>[29]</sup> In Mo<sub>2</sub>AlB<sub>2</sub>, the minimum peak-to-peak separation was 0.13 V for 0.1 mV s<sup>-1</sup> while the maximum value was 0.55 V for 2 mV s<sup>-1</sup>, which may indicate a decrease in reversibility for faster scan rates.<sup>[29]</sup> The general relationship between peak current and scan rate is given by  $i_p = av^b$  where  $a$  and  $b$  are adjustable parameters.<sup>[30]</sup> The  $b$ -value can range from ( $b = 0.5$ ) if the electrochemical reaction is limited by semi-infinite diffusion to ( $b = 1$ ) if the current is interface-controlled (typical for capacitive and pseudocapacitive systems).<sup>[31–33]</sup> Recording the upper peak

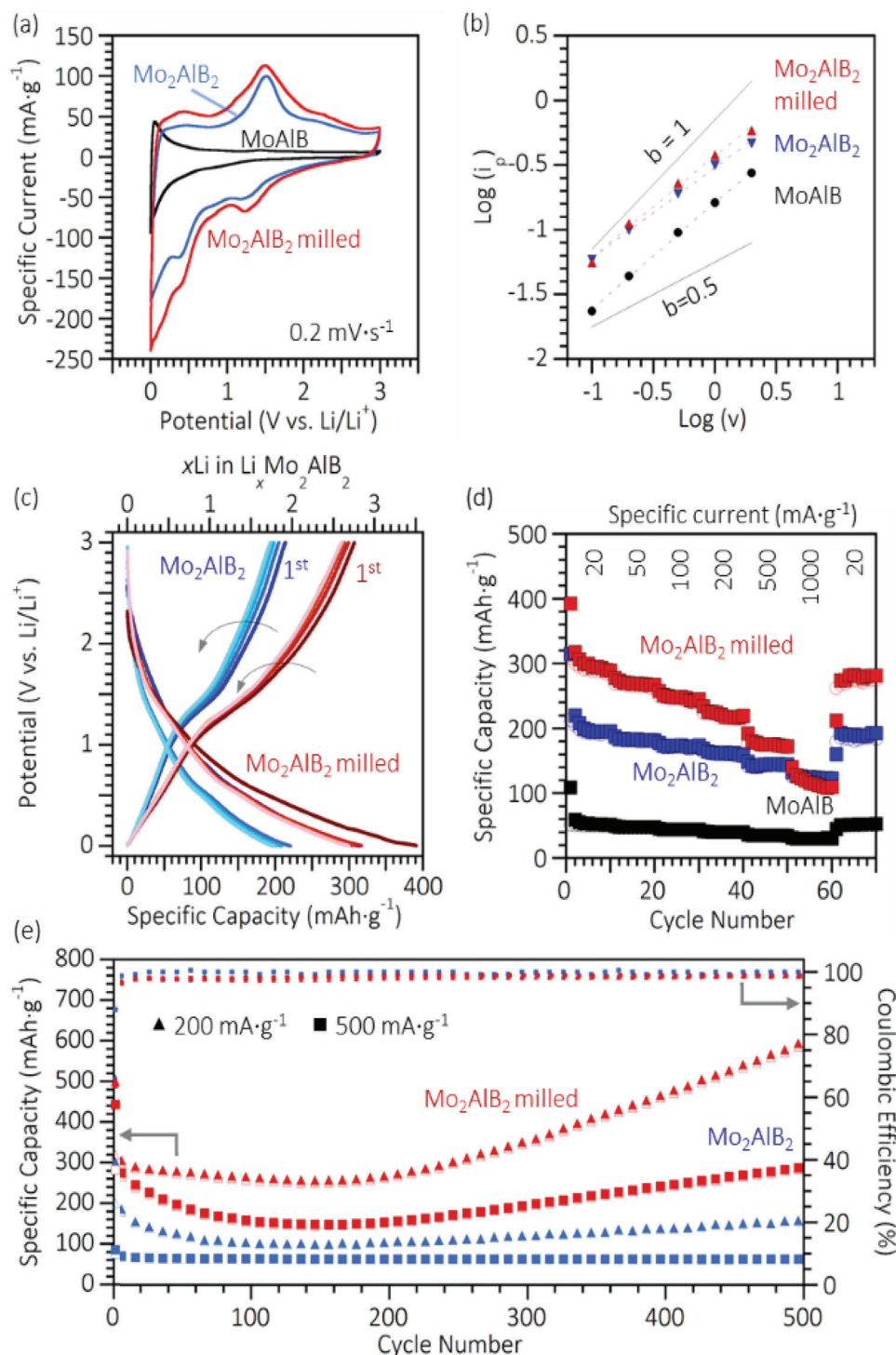


**Figure 2.** Electrochemical analysis. a) Cyclic voltammograms of MoAlB, Mo<sub>2</sub>AlB<sub>2</sub> before and after milling at 0.2 mV s<sup>-1</sup> scan rate. b) *b*-value  $\log(i_p) - \log(v)$  plot of voltammograms of MoAlB, Mo<sub>2</sub>AlB<sub>2</sub>, and milled Mo<sub>2</sub>AlB<sub>2</sub> tested at scan rates 0.1–2.0 mV s<sup>-1</sup>. c) Voltage profile of milled versus non-milled Mo<sub>2</sub>AlB<sub>2</sub> for the first five cycles at specific current 20 mA g<sup>-1</sup>. d) Rate handling capability of MoAlB, Mo<sub>2</sub>AlB<sub>2</sub>, and Mo<sub>2</sub>AlB<sub>2</sub> milled at specific currents of 20–1000 mA g<sup>-1</sup>. e) Cycling stability of non-milled and milled Mo<sub>2</sub>AlB<sub>2</sub> at specific currents of 200 and 500 mA g<sup>-1</sup>.



current values from each profile, we plotted  $\log(i_p)$  versus  $\log(v)$ , as shown in Figure 2b. After linear fitting, the  $b$  value for MoAlB, Mo<sub>2</sub>AlB<sub>2</sub>, and milled Mo<sub>2</sub>AlB<sub>2</sub> was 0.82, 0.70, and 0.78, respectively.

The voltage profile before and after milling is shown in Figure 2c, where the coin cell was cycled at 20 mA g<sup>-1</sup> and the first five cycles of each Mo<sub>2</sub>AlB<sub>2</sub> (blue profile) and Mo<sub>2</sub>AlB<sub>2</sub> milled (red profile). Both samples plateaued at ≈1.2 (discharge) and ≈1.5 V (charge) versus Li/Li<sup>+</sup>, which agrees with results obtained from cyclic voltammograms in Figure 2a. A specific capacity of 380 mAh g<sup>-1</sup> (3.5 Li per Mo<sub>2</sub>AlB<sub>2</sub>) was obtained in the first cycle of milled Mo<sub>2</sub>AlB<sub>2</sub>, which is 19% higher than the unmilled ones storing 320 mAh g<sup>-1</sup> (2.8 Li per Mo<sub>2</sub>AlB<sub>2</sub>). By the fifth cycle, milled Mo<sub>2</sub>AlB<sub>2</sub> had a 55% higher capacity of about 310 mAh g<sup>-1</sup> (2.7 Li) compared to the unmilled sample with a capacity of 200 mAh g<sup>-1</sup> (1.7 Li). Although the specific capacity of Mo<sub>2</sub>AlB<sub>2</sub> has not been reported before, the Mo<sub>2</sub>B<sub>2</sub> structure has been theoretically predicted to have a specific capacity of 444 mAh g<sup>-1</sup>, corresponding to 4 Li per Mo<sub>2</sub>B<sub>2</sub>. The difference between our reported values and the theoretical values of Mo<sub>2</sub>B<sub>2</sub> could be attributed to the incomplete removal of Al as singular Al layers exist in the Mo<sub>2</sub>AlB<sub>2</sub> structure.<sup>[12]</sup>

The rate handling was carried out at specific currents of 20–1000 mA g<sup>-1</sup> for MoAlB, Mo<sub>2</sub>AlB<sub>2</sub>, and Mo<sub>2</sub>AlB<sub>2</sub> milled in Figure 2d. In the first cycle, milled Mo<sub>2</sub>AlB<sub>2</sub> had a specific capacity about four times higher than MoAlB. The specific capacity for MoAlB was generally low (40–50 mAh g<sup>-1</sup>) in all tested specific currents. On the other hand, the capacity increased 230% and 300% for Mo<sub>2</sub>AlB<sub>2</sub>, and milled Mo<sub>2</sub>AlB<sub>2</sub>, respectively. At 20 mA g<sup>-1</sup>, milling the sample before testing increased the capacity 50%. The milling effect appeared to fade for higher specific currents until it vanished at a rate of 1000 mA g<sup>-1</sup>.

Exploring the cycling stability of Mo<sub>2</sub>AlB<sub>2</sub> in Figure 2e, we tested Mo<sub>2</sub>AlB<sub>2</sub> before and after milling at specific currents of 200 and 500 mA g<sup>-1</sup>. The first discharge specific capacity of the non-milled sample was 302 and 83 mAh g<sup>-1</sup> for specific currents 200 and 500 mA g<sup>-1</sup>, respectively. At 200 mA g<sup>-1</sup>, a minimum specific capacity was reached after 100 cycles; however, the capacity increased gradually with cycling reaching a specific capacity of 156 mAh g<sup>-1</sup> after 500 cycles. Milling Mo<sub>2</sub>AlB<sub>2</sub> had a beneficial effect on the specific capacity. For 200 and 500 mA g<sup>-1</sup> cells, the first discharge specific capacities of milled Mo<sub>2</sub>AlB<sub>2</sub> were 496 and 441 mAh g<sup>-1</sup>, respectively, which are 1.6- and 5.0-times higher than their respective non-milled. Coulombic efficiency for the first cycle was 68%, and after 20 cycles, it was maintained at >99%. After 500 cycles, the difference in capacity between milled and non-milled Mo<sub>2</sub>AlB<sub>2</sub> was significant and noticeable. The specific capacities of the milled ones were 594 and 283 mAh g<sup>-1</sup> at 200 and 500 mA g<sup>-1</sup>, respectively, which are 281% and 342% higher than the non-milled ones. The increase in specific capacity due to milling can be attributed to the decrease in average particle size, thereby increasing the accessible surface area and enabling more electrochemically active sites to store Li. The specific capacity values of milled Mo<sub>2</sub>AlB<sub>2</sub> are close to that of MXenes and commercial graphite in LIBs (372 mAh g<sup>-1</sup>). However, further studies to completely etch out the aluminum layer, will potentially increase the capacity.<sup>[3]</sup> The cycling-induced capacity enhancement was reported in previous literature.<sup>[34–39]</sup> Several reasons have been proposed to explain the anomalous ca-

capacity increase with cycling, including improved electrolyte wettability and creation of more accessible paths for shorter Li<sup>+</sup> ion migration,<sup>[34,35]</sup> the formation/decomposition of an electrolyte-derived surface layer, the possibility of additional charge storage at sharp interfaces between electronic and ionic sinks, redox reactions of Li-containing species, unconventional activity of structural defects, and metallic-cluster like Li storage.<sup>[38]</sup> Experimental evidence suggest that the reversible formation/decomposition of lithium oxide plays a major in the enhanced capacity upon long cycling.<sup>[39]</sup> However, further studies are needed to fully understand the reason behind this capacity increase in Mo<sub>2</sub>AlB<sub>2</sub> system. To shed light on the Li storage mechanism within Mo<sub>2</sub>AlB<sub>2</sub>, we used ex situ XRD before and after lithiation. The electrode was galvanostatically lithiated by discharging from open circuit potential to 1 mV versus Li/Li<sup>+</sup> at a specific current of 10 mA g<sup>-1</sup>, then maintained at 1 mV until disassembly; the voltage profile of the half cycle is shown in Figure 3a. The X-ray diffractogram after lithiation, in Figure 3b, shows no significant change in the (010) peak compared to the one before lithiation, suggesting that the storage mechanism is not likely to be intercalation. Furthermore, the absence of new reflections eliminates the possibility of a conversion reaction. The particles within the lithiated sample appeared to maintain their morphology without swelling, as shown in the scanning electron micrograph (inset, Figure 3a).

To investigate whether the higher performance of Mo<sub>2</sub>AlB<sub>2</sub> compared to MoAlB was related intrinsically to Mo<sub>2</sub>AlB<sub>2</sub>, not just due to oxides that might evolve during etching, we oxidized our material using rapid thermal annealing (RTA) by heating at 900 °C for 30 s in air. Figure S9a, Supporting Information, shows post-RTA XRD where MoO<sub>2</sub> (PDF#00-032-0671) and MoO<sub>3</sub> (PDF#00-067-0476) were observed, in addition to the significant unoxidized Mo<sub>2</sub>AlB<sub>2</sub>. If the performance were related to the oxides, it would be intuitive to assume that having more oxides would enhance the electrochemical performance and amplify the redox peaks. However, post-RTA cyclic voltammetry (CV) (Figure S9b, Supporting Information) revealed a cyclic voltammogram profile that can be distinguished from Mo<sub>2</sub>AlB<sub>2</sub> where three redox pairs were observed at (0.20 and 0.42 V), (1.25 and 1.42 V), and (1.54 and 1.72 V) versus Li/Li<sup>+</sup> which are related to both MoO<sub>2</sub> and MoO<sub>3</sub>.<sup>[40,41]</sup> The specific capacity decreased after oxidation; this suggests that plausible surface oxides are not responsible for the capacity we measured for Mo<sub>2</sub>AlB<sub>2</sub>.

We utilized XPS to explore the material's bonding and surface chemistry and probe changes, if any, in the oxidation state of Mo due to electrochemical cycling. The results are shown in Figure 3c and Table S2, Supporting Information. Four samples were used for the XPS study, namely, i) MoAlB before etching, ii) Mo<sub>2</sub>AlB<sub>2</sub> electrode before lithiation (MoAlB after HF etching), iii) Mo<sub>2</sub>AlB<sub>2</sub> electrode after lithiation, and iv) Mo<sub>2</sub>AlB<sub>2</sub> electrode after delithiation. In the Mo 3d spectra, a low binding energy peak at 228.0 eV that was observed in i) MoAlB can be assigned the 3d<sub>5/2</sub> of Mo–Al–B.<sup>[42]</sup> Other Mo 3d<sub>5/2</sub> peaks were observed at 229.5, 232.0, and 233.4 eV can be attributed to Mo(IV), Mo(V), and Mo(VI), respectively.<sup>[43]</sup> HF etching appeared to shift the Mo–Al–B 3d<sub>5/2</sub> peak to a higher binding energy of 228.4 eV, which could be attributed to the higher oxidation state of molybdenum after etching, similar to what was observed for MXenes.<sup>[44,45]</sup> The Mo–Al–B 3d<sub>5/2</sub> peak was observed at 227.8 eV for iii) fully lithiated (half cycle), and 228.2 eV for iv) fully lithiated and

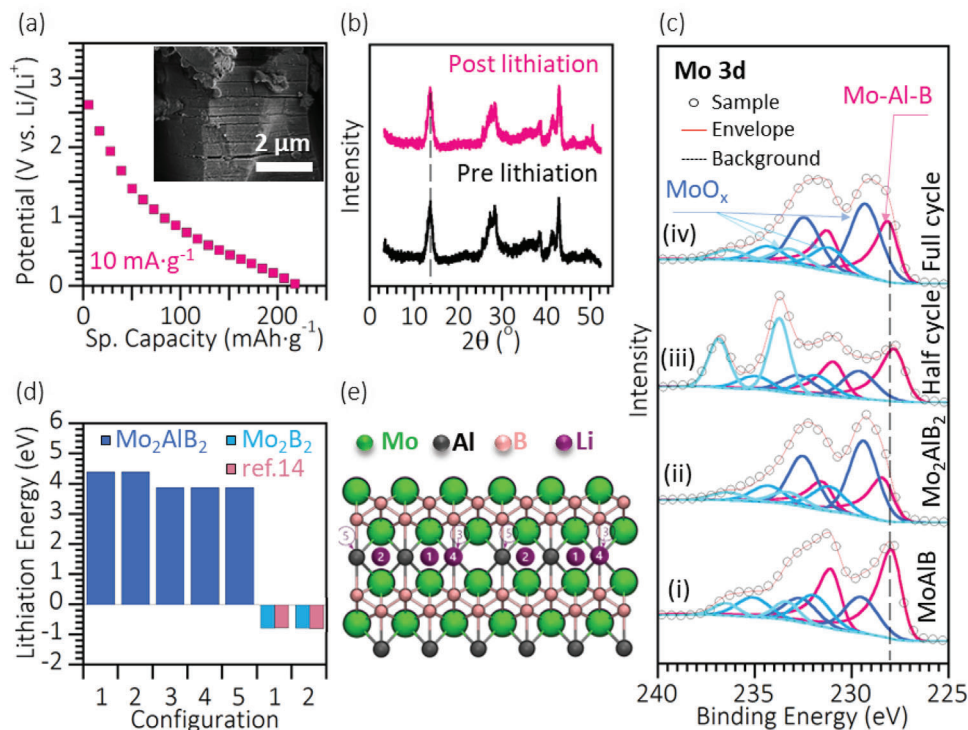


**Figure 3.**  $\text{Mo}_2\text{AlB}_2$  lithiation. a) Voltage profile of  $\text{Mo}_2\text{AlB}_2$  wafer during discharge at  $10 \text{ mA g}^{-1}$  with inset scanning electron micrograph of  $\text{Mo}_2\text{AlB}_2$  after lithiation. b) X-ray diffractograms before and after lithiation. c) XPS analysis of molybdenum spectrum for i)  $\text{MoAlB}$ ,  $\text{Mo}_2\text{AlB}_2$  electrode ii) before cycling, iii) half cycle, and iv) full cycle. d) DFT-calculated lithiation energies for varying Li configurations for  $\text{Mo}_2\text{AlB}_2$  and  $\text{Mo}_2\text{B}_2$  shown in (e) where the atomic structure of  $\text{Mo}_2\text{AlB}_2$  is shown with the different configurations where Mo = Green, Al = Black, B = Pink, and Li = Purple. More details about the atomic structure and Li configurations of  $\text{Mo}_2\text{AlB}_2$  and  $\text{Mo}_2\text{B}_2$  are shown in Figure S11, Supporting Information.

delithiated (full cycle). The lower binding energy of Mo-Al-B  $3d_{5/2}$  in the half cycle (after fully lithiated) suggests that  $\text{Mo}_2\text{AlB}_2$  is reduced by Li. This is direct evidence that  $\text{Mo}_2\text{AlB}_2$  is contributing to Li storage. The Mo-Al-B  $3d_{5/2}$  peak for the full-cycle sample partially recovered as it was shifted to a relatively higher binding energy (viz., higher oxidation state) compared to the half-cycle one, where 33% of the shift in binding energy was irreversible. This agrees with our electrochemical results of  $\text{Mo}_2\text{AlB}_2$  in Figure 2d, showing irreversibility in the first cycle from 300 to 200  $\text{mAh g}^{-1}$ . This irreversibility could be due to Li reaction with surface terminations or etching products. A summary of the XPS findings for Mo 3d can be found in Table S2, Supporting Information, in addition to C 1s, B 1s, Al 2p, O 1s, F 1s, and Li 1s high-resolution spectra shown in Figure S10, Supporting Information. From these results, we can conclude that the electrochemical performance observed in this study is intrinsic and related to the reversible redox reaction of Li with  $\text{Mo}_2\text{AlB}_2$  surface according to the following reaction:  $\text{Mo}_2\text{AlB}_2 + \gamma\text{Li}^+ + \gamma\text{e}^- \leftrightarrow \text{Li}_\gamma\text{Mo}_2\text{AlB}_2$ . Associating the higher Li storage with the milled sample suggests that Li was stored only at the surface of the particles. With milling, the particle size decreased, and relatively more surfaces were available to interact with lithium. To observe the effect of etching and milling treatments on the specific surface area (SSA) of  $\text{MoAlB}$  via nitrogen gas sorption analysis, as provided in Figure S12 and Table S3, Supporting Information. Although the SSA values are low for all samples ( $1\text{--}13 \text{ m}^2 \text{ g}^{-1}$ ), HF-etching raised the SSA values from 1 to  $7 \text{ m}^2 \text{ g}^{-1}$ . Further-

more, milling  $\text{Mo}_2\text{AlB}_2$  resulted in an increase of the SSA from 7 to  $13 \text{ m}^2 \text{ g}^{-1}$ .

To gain more insights into why Li does not intercalate in  $\text{Mo}_2\text{AlB}_2$  and is rather stored through surface redox, we carried out ab initio calculations. In the selection and use of MAB phases as electrode materials, the lithiation energy  $\Delta E_{\text{Li}}$  is a vital criterion for estimating the performance and the charge storage mechanism.<sup>[46]</sup> Therefore, we used DFT to calculate the lithiation energy into the bulk of  $\text{Mo}_2\text{AlB}_2$ . The structures in Figure 3e show the lowest energy configurations of both the pristine  $\text{Mo}_2\text{AlB}_2$  and lithiated  $\text{Mo}_2\text{AlB}_2$ . Our calculated lattice parameters were  $a = 3.06 \text{ \AA}$ ,  $b = 11.5 \text{ \AA}$ , and  $c = 3.18 \text{ \AA}$ , which match well with previous experimental work.<sup>[20]</sup> We tested five different intercalation configurations to find the most stable, as shown in Figure 3d. Our results indicate that Li is the most stable in the Al layer. In all these sites, the Li intercalation energy is positive ( $>3.8 \text{ eV}$ ), indicating that the Li atom is quite unstable. As a comparison, we also performed calculations for Li intercalation into  $\text{Mo}_2\text{B}_2$ , which has been studied previously. For  $\text{Mo}_2\text{B}_2$ , we calculate an intercalation energy of  $-0.77 \text{ eV}$ , in agreement with previous work.<sup>[14,47]</sup> Therefore, intercalation into bulk  $\text{Mo}_2\text{AlB}_2$  is more than 4 eV less favorable than  $\text{Mo}_2\text{B}_2$ . This suggests that intercalation into the bulk is unlikely to occur, in agreement with the XRD findings on the lithiated material.

Since Li storage is mostly due to the redox process at the surface of the layered borides and increasing the surface area by milling of  $\text{Mo}_2\text{AlB}_2$  results in higher specific capacity, it is

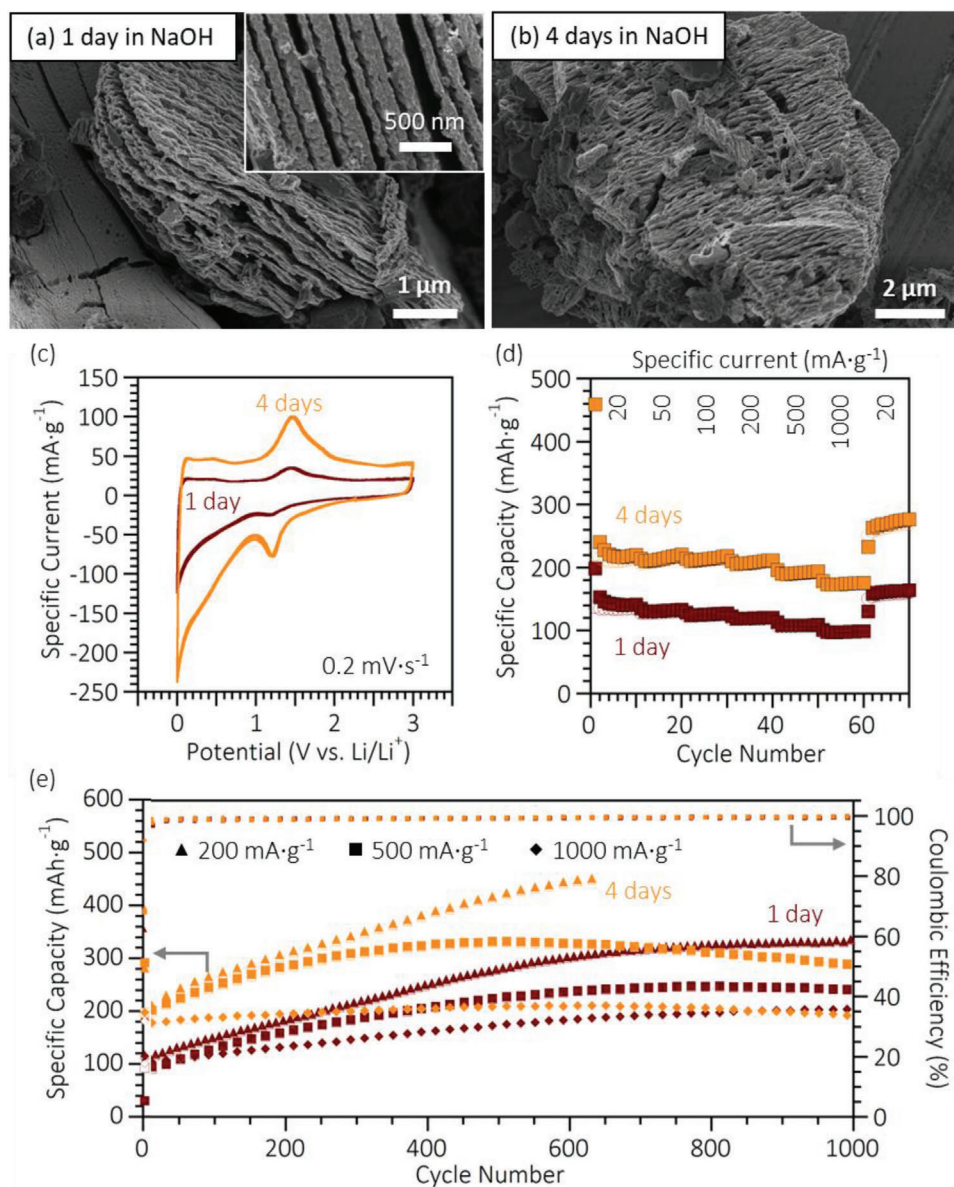


**Figure 4.** MoAlB + NaOH Scanning electron micrographs of MoAlB treated with NaOH for a) 1 and b) 4 days. Effect of NaOH treatment on the electrochemical behavior of MoAlB showing c) cyclic voltammograms of samples etched for 1 (brown color) and 4 days (orange color) at a  $0.2 \text{ mV s}^{-1}$  scan rate. d) Rate capability at specific currents of 20–1000  $\text{mA g}^{-1}$ . e) Cycling stability at 200, 500, and 1000  $\text{mA g}^{-1}$ .

reasonable to hypothesize that increasing the Li-accessible surface in MoAlB will have a similar effect to the etching and milling process in  $\text{Mo}_2\text{AlB}_2$ . Previous studies reported the effect of NaOH on MoAlB.<sup>[19–21]</sup> NaOH treatment was observed to etch the surface of MoAlB particles by removing the aluminum and forming  $\text{Mo}_2\text{AlB}_2$  on the surface with a MoAlB core.<sup>[20]</sup> Hence, we utilized NaOH to form  $\text{Mo}_2\text{AlB}_2$  surfaces and increase the SSA of MoAlB, as provided in Figure S12 and Table S3, Supporting Information. After treating MoAlB with NaOH for 1 and 4 days, the EDS analysis in Table S4, Supporting Information, showed a decrease in the Al content as the Mo:Al ratio changed from  $\approx 1.0:1.0$  to  $1.0:0.8$  after 1 day, and  $1.0:0.7$  after 4 days. A significant increase was noticed upon etching of the parent MoAlB

that has only  $1 \text{ m}^2 \text{ g}^{-1}$  SSA to  $4 \text{ m}^2 \text{ g}^{-1}$  for the 1 day-etched and to  $11 \text{ m}^2 \text{ g}^{-1}$  for the 4 days-etched samples.

The X-ray diffractograms, shown in Figure S13, Supporting Information, revealed no peak shift. However, a significant asymmetric broadening to higher  $2\theta$  was observed, particularly in the early (020) peak, which could be attributed to double peaks (MoAlB and  $\text{Mo}_2\text{AlB}_2$ ) or anisotropic strain. The emergence of shoulders and peak broadenings, which are observed in most of the peaks, are more pronounced upon longer NaOH treatment compared to that of parent MoAlB, in agreement with previous reports.<sup>[20]</sup> After NaOH treatment, scanning electron micrographs (Figure 4) show layered porous morphology. Since the formation of  $\text{Mo}_2\text{AlB}_2$  on the surface of MoAlB is a self-limiting



process, little visible difference can be observed from scanning electron micrographs of 1 day or 4 days treated samples. However, the distinction manifests itself in EDS (reduction of Al content) and XRD analyses outlined above. The particles were observed to be corrugated due to NaOH treatment. The layers were spaced out, and the surface roughness increased. We believe that both effects have a positive contribution to electrochemical activity.

Figure 4 shows the CVs of MoAlB treated in NaOH for 1 day and 4 days. Both voltammograms show redox peaks at (1.2 and 1.5 V); comparable to redox peaks for HF-etched Mo<sub>2</sub>AlB<sub>2</sub> in Figure 2. PEIS of 1 day versus 4 days NaOH-treated MoAlB are shown in Figure S4b, Supporting Information, where the circuit used for fitting is shown in Figure S4c, Supporting Information. We observed that for 1 and 4 days,  $R_s$  was 0.11 and 0.06 mΩ cm<sup>2</sup>, respectively. For the charge transfer resistance,  $R_{ct}$ , was 4.5 and 4.1 mΩ cm<sup>2</sup> for 1 day and 4 days, respectively. The longer treatment appeared to reduce the system and charge transfer resistance. Recording the upper peak current values from each profile, we plotted log( $i_p$ ) versus log( $v$ ), as shown in Figure S4d, Supporting Information. After linear fitting, the  $b$ -values for MoAlB before and after NaOH treated for 1 day and 4 days were 0.82, 0.82, and 0.85, respectively. The rate handling capability in Figure 4d shows a significant increase in specific capacity after treating for 4 days, compared to 1 day. A specific capacity of 460 mAh g<sup>-1</sup> was achieved in the first discharge cycle of the 4 days sample, which is more than double the capacity of the 1 day sample. At 20 mA g<sup>-1</sup>, HF-treated samples appeared to have a higher specific capacity. However, at a higher specific current of 1000 mA g<sup>-1</sup>, the 4 days NaOH-treated sample exceeded both the milled and non-milled HF-treated samples. NaOH-treated samples showed a slight loss in the specific capacity by doubling the specific current from 500 to 1000 mA g<sup>-1</sup>. In addition, the specific capacity appeared to increase with the ten cycles under constant specific current, especially when comparing the samples when cycled at 20 mA g<sup>-1</sup> at the beginning and the end of the test.

The cycling stability of NaOH-treated samples, shown in Figure 4e, confirms the significantly enhanced specific capacity. The electrodes were cycled at specific currents of 200, 500, and 1000 mA g<sup>-1</sup>. After 500 cycles, the specific capacity of the 4 days NaOH treated sample was 420, 332, and 209 mAh g<sup>-1</sup> for cells tested under specific currents of 200, 500, and 1000 mA g<sup>-1</sup>, respectively. The 1 day NaOH treated sample showed 280, 225, and 174 mAh g<sup>-1</sup> for the same respective specific currents. At 500 mA g<sup>-1</sup>, both NaOH-treated samples have higher specific capacity than the non-milled HF-treated samples; however, not as high as the milled HF-treated samples.

Due to the abundance and low cost of sodium, SIBs are explored as a more sustainable alternative to LIBs. Hence, we incorporated our material into SIBs to test their performance, as shown in Figure S8, Supporting Information. The cyclic voltammogram (Figure S8a, Supporting Information) from cycling at 0.1 mV s<sup>-1</sup> for 20 cycles shows that the redox peaks shifted significantly to lower values <1 V versus Na/Na<sup>+</sup>. However, the capacity gradually decreased with more cycling. Rate capability was also tested at the same specific currents as before (Figure S8b, Supporting Information). The maximum capacity was 150 mAh g<sup>-1</sup> at 20 mA g<sup>-1</sup>, gradually decreasing with higher specific currents. The electrode showed good capacity retention when tested

at 20 mA g<sup>-1</sup> again after cycling at higher rates. Figure S8c, Supporting Information, shows the voltage profile of the first five cycles of Figure S8b, Supporting Information, where the capacity started low then gradually increased with more cycling. The measured specific capacity corresponds to 1 Na per Mo<sub>2</sub>AlB<sub>2</sub> formula unit. Although the capacity values reported for the SIB are not as high as that for the LIB, the results confirm the feasibility of storing both Li and Na in layered molybdenum borides.

Based on the experimental work we presented, it was found that the as-furnaced MoAlB has low SSA (Figure S12 and Table S3, Supporting Information) and low specific capacity (Figure 2). Etching MoAlB either by HF or NaOH increased the SSA (Figure S12 and Table S3, Supporting Information) and electrochemical performance, Figures 2 and 4). Although increasing the electroactive surface area may facilitate side reactions like SEI formation, studies show it can improve battery performance.<sup>[48]</sup> Among the etched samples, NaOH-treated MoAlB (4 days) and HF-etched-milled MoAlB exhibited high SSAs,  $b$ -values, capacitive contribution percentages, and, consequently, high energy storage capacities.

Structurally, HF-etching fully transformed MoAlB to Mo<sub>2</sub>AlB<sub>2</sub>, as shown in Figure 1. NaOH treatment was less aggressive than HF acid. It was enough to etch only the surface of MoAlB particles and form Mo<sub>2</sub>AlB<sub>2</sub> surfaces; however, the core is still MoAlB (Figure S13, Supporting Information) which agrees with previous results.<sup>[20]</sup> From a surface area point of view, HF-etching resulted in a higher SSA than MoAlB, and milling further increased the SSA significantly by reducing the particle size. 1 day NaOH treatment increased surface area of MoAlB, and extending the NaOH treatment to 4 days significantly increased the surface area even more (Figure S12 and Table S3, Supporting Information).

To confirm that the electrochemical redox reactions are surface-controlled, we analyzed the voltammograms at different scan rates. HF-etched MoAlB had the lowest  $b$ -value of 0.7 (Figure 2 and Figure S4, Supporting Information), indicating a stronger limitation by diffusion of the species entering and leaving the electrode surface. Milling Mo<sub>2</sub>AlB<sub>2</sub> increased the  $b$ -value due to exposing more surfaces via particle size reduction. 4 days NaOH-treated MoAlB had the highest  $b$ -value of 0.85 (Figure 2 and Figure S4, Supporting Information). The capacitive contribution at scan rates 0.2 and 2.0 mV s<sup>-1</sup> are shown in Figures S5–S7, Supporting Information. The surface-controlled contribution appeared to increase due to milling the HF-etched MoAlB and extending NaOH treatment from 1 to 4 days.

### 3. Conclusions

In conclusion, we successfully synthesized the Mo<sub>2</sub>AlB<sub>2</sub> structure, which is one step closer to the Mo<sub>2</sub>B<sub>2</sub> MBene than MoAlB. We used solid-state synthesis to produce the Mo<sub>2</sub>AlB<sub>2</sub> precursor (i.e., MoAlB), which was then partially etched to remove 50% of Al using HF acid at 45 °C for 2 days. The etching process caused significant changes in XRD, morphology, and EDS. When we tested the materials as electrodes for Li-ion battery, we found that the specific capacity of the first discharge was quadrupled when milled Mo<sub>2</sub>AlB<sub>2</sub> was used instead of MoAlB. After 500 cycles, specific capacities 594 and 302 mAh g<sup>-1</sup> were obtained for milled Mo<sub>2</sub>AlB<sub>2</sub> and non-milled Mo<sub>2</sub>AlB<sub>2</sub>, respectively, when tested at 200 mA g<sup>-1</sup>. Ex situ XRD and XPS studies for electrochemically

lithiated and delithiated samples were performed to understand the underlying charge storage mechanism. XRD showed no shift in (010) peaks even for Li discharge capacity of  $>200 \text{ mAh g}^{-1}$ , suggesting that the charge storage is not by ion intercalation. This aligns with DFT calculations, showing unfavorable Li intercalation in  $\text{Mo}_2\text{AlB}_2$ . XPS was used to understand the bonding nature after etching, lithiation, and delithiation. The binding energy of the Mo–Al–B peak in the Mo 3d spectra was found to be shifted to higher values due to etching, lower due to lithiation, and higher again due to delithiation. NaOH treatment of MoAlB resulted in a corrugated porous morphology with layers of high surface roughness. NaOH-treated MoAlB has a significantly higher specific capacity compared to  $\text{Mo}_2\text{AlB}_2$ . Specific capacities of 420, 332, and 200  $\text{mAh g}^{-1}$  were achieved for 4 days NaOH-treated samples tested under specific currents of 200, 500, and 1000  $\text{mA g}^{-1}$ , respectively. When  $\text{Mo}_2\text{AlB}_2$  was tested in Na-ion batteries, a specific capacity of 150  $\text{mAh g}^{-1}$  was obtained at 20  $\text{mA g}^{-1}$  suggesting potential applications in electrochemical energy storage beyond Li-ion batteries. The present work highlights the viability of transition metal borides as electrode materials for ion batteries. It suggests further studies to realize borides and explore other layered transition metal boride systems for energy storage.

#### 4. Experimental and Methods Section

**Synthesis of MoAlB Powder:** The MoAlB powder was synthesized by mixing and heating molybdenum boride (MoB,  $<45 \mu\text{m}$ , 99%, Alfa Aesar) and aluminum (Al,  $<45 \mu\text{m}$ , 99.5%, Alfa Aesar) with atomic ratio Mo:B:Al of 1:1.2. For mixing, zirconia balls were added with the powders into a high-density polyethylene (HDPE) bottle that was then loaded to a Turbula T2F mixer and rotated at 56 rpm for 3 h. Afterward, the mixture was cold-pressed into a 1 in. diameter pellet and put into an alumina crucible in the center of an alumina tube furnace. The pellet was heated from room temperature to 750 °C, held for 2 h, then heated to 1550 °C for 2 h, and finally cooled naturally to room temperature. A heating rate of 10 °C  $\text{min}^{-1}$  was used throughout the heating steps, and the whole thermal cycle was performed under constant argon (Ar) gas flow.

**Synthesis of  $\text{Mo}_2\text{AlB}_2$ :**  $\text{Mo}_2\text{AlB}_2$  phase was synthesized by partial selective etching of Al from the MoAlB phase. The MoAlB pellet was ground into powders ( $<45 \mu\text{m}$ ) and then added to a bottle containing hydrofluoric acid (HF, 48–51 mass%, Acros Organics, CAS: 7664-39-3) at a MoAlB:HF ratio of (1 g:10 mL). The latter was done by carefully following the strict safety protocols for handling HF.<sup>[49]</sup> During the initial step of adding powders to the solution, the bottle was submerged in an ice bath. The mixture was then heated to 45 °C inside a bath of mineral oil and held at this temperature for 48 h with continuous stirring using a polytetrafluoroethylene-coated magnetic bar at  $\approx 500 \text{ rpm}$ . Afterward, the powders were washed using de-ionized (DI) water through centrifuging at 3500 rpm for 5 min, decanting the supernatant, and refilling with DI water. The washing steps were repeated until a near-neutral pH level ( $>6$ ) was achieved, and finally, the powders were dried using vacuum-assisted filtration. To reduce the particle size, zirconia balls were added to the  $\text{Mo}_2\text{AlB}_2$  powders into a 15 mL HDPE bottle filled with absolute ethanol (200 Proof, meets USP/EP/ACS, Fisher Chemical). The bottle was sealed and inserted into a high-energy ball milling (8000 m Mixer/Mill High-Energy Ball Mill, SPEX SamplePrep) for six cycles (5 min each). After 5 min of milling, the HDPE bottle was cooled in an ice bath. Afterward, the milled powders were collected and dried through vacuum-assisted filtration.

**MoAlB Particle Size Selection before Etching:** To narrow the particle size distribution of MoAlB before etching, we followed a procedure similar to that reported by Zhang et al.,<sup>[26]</sup> where the ground MoAlB powder with particle size  $<45 \mu\text{m}$  was put into a bath sonication with DI water for 20 min to deagglomerate particles and then the mixture was stirred to maintain

uniform distribution. Once stirring was stopped, powders in DI water were allowed to settle for 154 s to sediment particles in the range of 10–45  $\mu\text{m}$ , and the particles  $<10 \mu\text{m}$  were filtered from the supernatant.

**NaOH Treatment of MoAlB:** The NaOH treatment of MoAlB powders was performed following a procedure reported elsewhere.<sup>[21]</sup> Typically, 250 mg of MoAlB was treated with 250 mL of 10 mass% NaOH solution (Sigma-Aldrich) at RT for 1 day (24 h) or 4 days (96 h) under stirring. Afterward, the mixture was vacuum-filtered through polyvinylidene fluoride (PVDF) membranes (0.22  $\mu\text{m}$ , Merck Durapore), followed by filtration of an excessive amount of DI water to wash away residual NaOH. The wet PVDF membrane with the powder cake on its top was then placed in a vacuum oven at room temperature overnight. The dried powder was then gently removed from the membrane and stored to be used as electrode material.

**Material Characterization:** The crystal structure of the samples was investigated using a Cu  $K_\alpha$  Rigaku D/Max-2200 X-ray diffractometer. X-ray diffraction patterns were collected at a  $2\theta$  step size of 0.02° and scan rate of 1°  $\text{min}^{-1}$ . Scanning electron microscopy (SEM) images were captured using either an INCA-Hitachi S-4800 at an acceleration voltage of 3 kV, or a ZEISS-Gemini SEM500 system with acceleration voltages between 1–3 kV. The chemical composition within each sample was obtained through EDS via the INCA-Hitachi S-3400 at an accelerating voltage of 30 kV. The XPS measurements were performed using the K-Alpha XPS System from Thermo Scientific. The photon source was a monochromatized Al X-Ray source (1.486 keV). The spectra were acquired using a spot size of 300  $\mu\text{m}$  and constant pass energy (150 eV for a survey and 20 eV for high-resolution spectra). A combined low-energy electron/ion flood source was used for charge neutralization. A dual monoatomic and gas cluster Ar ion source was adopted for depth profiling and sample cleaning. A vacuum transfer vessel was used to protect the sample from oxidation. To clean the sample surface from contamination, Ar sputtering was applied onto MoAlB powder,  $\text{Mo}_2\text{AlB}_2$ , lithiated  $\text{Mo}_2\text{AlB}_2$ , and delithiated  $\text{Mo}_2\text{AlB}_2$  for 30, 360, 600, and 360 s, respectively. More sputtering time was required for the lithiated  $\text{Mo}_2\text{AlB}_2$  to remove the SEI layer. The X-ray photoelectron spectra were calibrated using adventitious carbon at 284.8 eV.<sup>[50]</sup> Linear and Shirley backgrounds were used for C 1s and Mo 3d, respectively. Most peaks were fitted using a Gaussian Lorentzian curve GL(30), except for Mo–Al–B which was fit using A(0.38,0.6,10)GL(10), assuming peak asymmetry. The Mo 3d high-resolution spectrum was fitted using doublets  $3d_{5/2}$  and  $3d_{3/2}$  with an area ratio 3:2 and separated by 3.13 eV.

**Electrochemical Testing:** LIBs with  $\text{Mo}_2\text{AlB}_2$  as an active material were assembled to study their electrochemical performance. The slurry was prepared using the active material, carbon black (CB, Alfa Aesar,  $>99.9\%$ ), and PVDF (molecular weight  $\approx 534\,000$ , Sigma-Aldrich) in a mass ratio of 8:1:1, respectively. 1-Methyl-2-pyrrolidone (99.5%, Acros Organics, extra dry over molecular sieve) was added to the mixture and ground together using mortar and pestle until a homogeneous slurry was formed. The slurry was drop cast using a pipette on copper foil discs (10  $\mu\text{m}$  thick, 12 mm diameter) and allowed to dry overnight in an oven at 60 °C. In the standard two-electrode CR2032 coin cells used in this study, the active material acted as a working electrode, and lithium/sodium metal acted as a counter and reference electrode. For LIBs, 1 M lithium hexafluorophosphate ( $\text{LiPF}_6$ ) dissolved in ethylene carbonate (EC) and ethyl methyl carbonate (EMC) EC:EMC (3:7 by volume) was used on the glass fiber separator, while for SIBs, 1 M sodium hexafluorophosphate ( $\text{NaPF}_6$ ) dissolved in ethylene carbonate (EC) and diethyl carbonate (DEC) EC:DEC (1:1 by volume) was used. Coin cells assembly was carried out in an Ar-filled glovebox ( $\text{O}_2$  and  $\text{H}_2\text{O} <0.1 \text{ ppm}$ ).

CV and PEIS tests in this study were performed at room temperature using an electrochemical workstation (VMP3, BioLogic), and EC-Lab software was utilized for data collection and analysis. CV was measured at scan rates of 0.1, 0.2, 0.5, 1.0, and 2.0  $\text{mV s}^{-1}$  between 1 mV and 3 V versus  $\text{Li/Li}^+$  (for SIB, the voltages are measured versus  $\text{Na/Na}^+$ ). 200 kHz to 10 mHz was the frequency range for PEIS test. Galvanostatic cycling for rate handling capability and stability tests were performed by battery cycler (CT2001A, LANDHE, Wuhan, China). The rate handling capability was quantified using specific currents of 20, 50, 100, 200, 500, 1000, and

back to 20 mA g<sup>-1</sup>. Cycling stability was studied at specific currents of 100, 200, 500, and 1000 mA g<sup>-1</sup>.

**Gas Sorption Analysis:** Nitrogen gas sorption analysis was performed using an Autosorb iQ system (Quantachrome; now Anton-Paar) at liquid nitrogen temperature (−196 °C). Before each measurement, the samples in test tubes were outgassed by heating mantles that heated the samples at a ramping rate of 20 °C min<sup>-1</sup> to reach the target temperature of 300 °C and held for 3 h. The SSA was calculated by the ASiQwin-software using the Brunauer–Emmett–Teller equation<sup>[51]</sup> and quenched-solid DFT.<sup>[52]</sup>

**Theoretical Calculations:** Density functional theory (DFT) calculations were carried out using the Vienna ab initio simulation package.<sup>[53,54]</sup> The generalized gradient approximation of Perdew, Burke, and Ernzerhof, was utilized for the exchange–correlation functional.<sup>[55]</sup> The projector-augmented wave method was used to treat the electron–ion interaction, and the cut-off energy of the plane-wave basis set was 550 eV. A 3 × 3 × 1 cell of Mo<sub>2</sub>AlB<sub>2</sub> was employed to model the intercalation of Li using a 4 × 4 × 1 k-point grid.<sup>[56,57]</sup>

We performed a full geometry optimization for the Li-incorporated Mo<sub>2</sub>AlB<sub>2</sub>, placing the Li in multiple sites to find the most favorable configuration. The energy for Li intercalation was calculated as

$$\Delta E_{\text{Li}} = E_{\text{Mo}_2\text{AlB}_2+\text{Li}_n} - E_{\text{Mo}_2\text{AlB}_2} - nE_{\text{Li}} \quad (1)$$

Here,  $E_{\text{Mo}_2\text{AlB}_2+\text{Li}_n}$  is the total energy of the lithiated Mo<sub>2</sub>AlB<sub>2</sub> with  $n$  Li atoms,  $E_{\text{Mo}_2\text{AlB}_2}$  represents the total energy of the pristine Mo<sub>2</sub>AlB<sub>2</sub>, and  $E_{\text{Li}}$  denotes the total energy per atom of bulk Li metal. A negative value of the intercalation energy indicates that the Li atom prefers to intercalate into the Mo<sub>2</sub>AlB<sub>2</sub> rather than Li cluster formation.<sup>[12]</sup> In this work, our calculated lattice parameters were  $a = 3.06$  Å,  $b = 11.5$  Å, and  $c = 3.18$  Å, which match well with previous experimental work.<sup>[20]</sup>

## Supporting Information

Supporting Information is available from the Wiley Online Library or from the author.

## Acknowledgements

This work was supported by the National Science Foundation under Grant No. DMR-2048164. M.T. and V.P. acknowledge funding by the German Research Foundation (DFG, Deutsche Forschungsgemeinschaft) of the MXene-CDI project (PR-1173/11). C.D. and J.J.U. acknowledge funding by the Work at the Molecular Foundry supported by the Office of Science, Office of Basic Energy Sciences, of the U.S. Department of Energy under Contract No. DE-AC02-05CH11231. C.F.N. gratefully acknowledges support from the Tulane University.

## Conflict of Interest

The authors declare no conflict of interest.

## Data Availability Statement

The data that support the findings of this study are available from the corresponding author upon reasonable request.

## Keywords

layered materials, lithium-ion batteries, molybdenum boride

Received: February 13, 2023  
Revised: April 19, 2023  
Published online: May 18, 2023

- [1] Y. Nishi, *J. Power Sources* **2001**, *100*, 101.
- [2] Y. S. Zhang, N. E. Courtier, Z. Zhang, K. Liu, J. J. Bailey, A. M. Boyce, G. Richardson, P. R. Shearing, E. Kendrick, D. J. L. Brett, *Adv. Energy Mater.* **2021**, *12*, 2.
- [3] D. Er, J. Li, M. Naguib, Y. Gogotsi, V. B. Shenoy, *ACS Appl. Mater. Interfaces* **2014**, *6*, 11173.
- [4] J. Liu, X. W. Liu, *Adv. Mater.* **2012**, *24*, 4097.
- [5] Q. Gu, G. Krauss, W. Steurer, *Adv. Mater.* **2008**, *20*, 3620.
- [6] C. Martini, G. Palombarini, G. Poli, D. Prandstraller, *Wear* **2004**, *256*, 608.
- [7] X. Yu, S. Licht, *J. Power Sources* **2008**, *179*, 407.
- [8] H. Vrubel, X. Hu, *Angew. Chem., Int. Ed. Engl.* **2012**, *51*, 12703.
- [9] W. G. Fahrenholtz, G. E. Hilmas, *Int. Mater. Rev.* **2013**, *57*, 61.
- [10] L. Verger, S. Kota, H. Roussel, T. Ouisse, M. W. Barsoum, *J. Appl. Phys.* **2018**, *124*, 205108.
- [11] M. Naguib, M. W. Barsoum, Y. Gogotsi, *Adv. Mater.* **2021**, *33*, 2103393.
- [12] Z. Guo, J. Zhou, Z. Sun, *J. Mater. Chem.* **2017**, *5*, 23530.
- [13] V. G. Nair, M. Birowska, D. Bury, M. Jakubczak, A. Rosenkranz, A. M. Jastrzębska, *Adv. Mater.* **2022**, *34*, 2108840.
- [14] T. Bo, P. F. Liu, J. Zhang, F. Wang, B. T. Wang, *Phys. Chem. Chem. Phys.* **2019**, *21*, 5178.
- [15] J. Jia, B. Li, S. Duan, Z. Cui, H. Gao, *Nanoscale* **2019**, *11*, 20307.
- [16] M. Zhang, H. Wang, H. Wang, T. Cui, Y. Ma, *Phys. Chem. Chem. Phys.* **2010**, *144*, 6722.
- [17] M. Naguib, V. N. Mochalin, M. W. Barsoum, Y. Gogotsi, *Adv. Mater.* **2014**, *26*, 992.
- [18] W. Jeitschko, *Monatsh. Chem.* **1966**, *97*, 1472.
- [19] L. T. Alameda, C. F. Holder, J. L. Fenton, R. E. Schaak, *Chem. Mater.* **2017**, *29*, 8953.
- [20] L. T. Alameda, R. W. Lord, J. A. Barr, P. Moradifar, Z. P. Metzger, B. C. Steimle, C. F. Holder, N. Alem, S. B. Sinnott, R. E. Schaak, *J. Am. Chem. Soc.* **2019**, *141*, 10852.
- [21] L. T. Alameda, P. Moradifar, Z. P. Metzger, N. Alem, R. E. Schaak, *J. Am. Chem. Soc.* **2018**, *140*, 8833.
- [22] K. Kim, C. Chen, D. Nishio-Hamane, M. Okubo, A. Yamada, *Chem. Commun.* **2019**, *55*, 9295.
- [23] J. Zhou, J. Palisaitis, J. Halim, M. Dahlqvist, Q. Tao, I. Persson, L. Hultman, P. O. Å. Persson, J. Rosen, *Science* **2021**, *373*, 801.
- [24] N. F. Rosli, M. Z. M. Nasir, N. Antonatos, Z. Sofer, A. Dash, J. Gonzalez-Julian, A. C. Fisher, R. D. Webster, M. Pumera, *ACS Appl. Nano Mater.* **2019**, *2*, 6010.
- [25] Y. Zhou, H. Xiang, H. Zhang, F.-Z. Dai, *J. Mater. Sci. Technol.* **2019**, *35*, 2926.
- [26] J. Zhang, N. Kong, S. Uzun, A. Levitt, S. Seyedin, P. A. Lynch, S. Qin, M. Han, W. Yang, J. Liu, X. Wang, Y. Gogotsi, J. M. Razal, *Adv. Mater.* **2020**, *32*, 2001093.
- [27] S. Kota, E. Zapata-Solvas, A. Ly, J. Lu, O. Elkassabany, A. Huon, W. E. Lee, L. Hultman, S. J. May, M. W. Barsoum, *Sci. Rep.* **2016**, *6*, 26475.
- [28] K. Yu, J. Li, H. Qi, C. Liang, *Diamond Relat. Mater.* **2018**, *86*, 139.
- [29] N. Elgrishi, K. J. Rountree, B. D. McCarthy, E. S. Rountree, T. T. Eisenhart, J. L. Dempsey, *J. Chem. Educ.* **2017**, *95*, 197.
- [30] H. Lindström, S. Södergren, A. Solbrand, H. Rensmo, J. Hjelm, A. Hagfeldt, S. E. Lindquist, *J. Phys. Chem. B* **1997**, *101*, 7717.
- [31] V. Augustyn, E. R. White, J. Ko, G. Grüner, B. C. Regan, B. Dunn, *Mater. Horiz.* **2014**, *1*, 219.
- [32] S. Fleischmann, J. B. Mitchell, R. Wang, C. Zhan, D. E. Jiang, V. Presser, V. Augustyn, *Chem. Rev.* **2020**, *120*, 6738.
- [33] M. Opitz, J. Yue, J. Wallauer, B. Smarsly, B. Roling, *Electrochim. Acta* **2015**, *168*, 125.
- [34] Y. Xie, H. Zou, H. Xiang, R. Xia, D. Liang, P. Shi, S. Dai, H. Wang, *J. Membr. Sci.* **2016**, *503*, 25.

- [35] C. Gao, Z. Jiang, S. Qi, P. Wang, L. R. Jensen, M. Johansen, C. K. Christensen, Y. Zhang, D. B. Ravnsbaek, Y. Yue, *Adv. Mater.* **2022**, *34*, 2110048.
- [36] T. B. Schon, S. Y. An, A. J. Tilley, D. S. Seferos, *ACS Appl. Mater. Interfaces* **2019**, *11*, 1739.
- [37] J. Guo, Y. Li, J. Meng, K. Pedersen, L. Gurevich, D.-I. Stroe, *J. Energy Chem.* **2022**, *74*, 34.
- [38] H. Kim, W. Choi, J. Yoon, J. H. Um, W. Lee, J. Kim, J. Cabana, W.-S. Yoon, *Chem. Rev.* **2020**, *120*, 6934.
- [39] Y. Huang, Z. Xu, J. Mai, T.-K. Lau, X. Lu, Y.-J. Hsu, Y. Chen, A. C. Lee, Y. Hou, Y. S. Meng, *Nano Energy* **2017**, *41*, 426.
- [40] W. Wang, J. Qin, Z. Yin, M. Cao, *ACS Nano* **2016**, *10*, 10106.
- [41] L. C. Yang, Q. S. Gao, Y. Tang, Y. P. Wu, R. Holze, *J. Power Sources* **2008**, *179*, 357.
- [42] V. Natu, S. S. Kota, M. W. Barsoum, *J. Eur. Ceram. Soc.* **2020**, *40*, 305.
- [43] T. Zhang, C.-Y. Lee, B. Gong, B. Hoex, *AIP Conf. Proc.* **2018**, *1999*, 040027.
- [44] J. Halim, K. M. Cook, M. Naguib, P. Eklund, Y. Gogotsi, J. Rosen, M. W. Barsoum, *Appl. Surf. Sci.* **2016**, *362*, 406.
- [45] L.-Å. Näslund, P. O. Å. Persson, J. Rosen, *J. Phys. Chem.* **2020**, *124*, 27732.
- [46] P. Xiao, N. Jin, Z. Lin, *Mater. Res. Lett.* **2021**, *9*, 516.
- [47] Y. Xiao, Y. Li, Z. Guo, C. Tang, B. Sa, N. Miao, J. Zhou, Z. Sun, *Appl. Surf. Sci.* **2021**, *566*, 150634.
- [48] X. Han, L. Lu, Y. Zheng, X. Feng, Z. Li, J. Li, M. Ouyang, *eTransportation* **2019**, *1*, 100005.
- [49] C. E. Shuck, K. Ventura-Martinez, A. Goad, S. Uzun, M. Shekhirev, Y. Gogotsi, *ACS Chem. Health Saf.* **2021**, *28*, 326.
- [50] G. Schön, *J. Electron Spectrosc. Relat. Phenom.* **1972**, *1*, 377.
- [51] S. Brunauer, P. H. Emmett, E. Teller, *J. Am. Chem. Soc.* **1938**, *60*, 309.
- [52] G. Y. Gor, M. Thommes, K. A. Cychosz, A. V. Neimark, *Carbon* **2012**, *50*, 1583.
- [53] G. Kresser, J. Furthmüller, *Comput. Mater. Sci.* **1996**, *6*, 15.
- [54] G. Kresse, J. Hafner, *Phys. Rev. B: Condens. Matter Mater. Phys.* **1993**, *47*, 558.
- [55] J. P. Perdew, K. Burke, M. Ernzerhof, *Phys. Rev. Lett.* **1996**, *77*, 3865.
- [56] G. Kresse, D. Joubert, *Phys. Rev. B* **1999**, *59*, 1758.
- [57] P. E. Blöchl, *Phys. Rev. B* **1994**, *50*, 17953.